Article:
Walling, SA, Bernal, SA, Gardner, LJ et al. (2 more authors) (2018) Phase Formation and Evolution in $Mg(OH)_2$–Zeolite Cements. Industrial & Engineering Chemistry Research, 57 (6). pp. 2105-2113. ISSN 0888-5885

https://doi.org/10.1021/acs.iecr.7b04201

Phase formation and evolution in $Mg(OH)_2$ - zeolite cements

*Sam A. Walling, Susan A. Bernal, Laura J. Gardner, Hajime Kinoshita, John L. Provis**

Immobilisation Science Laboratory, Department of Materials Science & Engineering, The University of Sheffield, S1 3JD, UK

* Corresponding author. Tel: +44 (0) 114 222 5490, email: j.provis@sheffield.ac.uk

Abstract

The mineralogy and structure of cements in the system $Mg(OH)_2$-$NaAlO_2$-SiO_2-H_2O are investigated, with a view toward potential application in the immobilisation of $Mg(OH)_2$-rich Magnox sludges resulting from historic UK nuclear operations. The reaction process leading to the formation of these aluminosilicate binders is strongly exothermic, initially forming zeolite NaA (LTA structure), which is metastable in low SiO_2/Al_2O_3 binders, slowly evolving into the more stable sodalite and faujasite framework types. Notable chemical reaction of $Mg(OH)_2$ was only identified in the formulation with SiO_2/Al_2O_3 =1.3 (the lowest molar ratio among those tested), after extended curing times. In this case, some of the $Mg(OH)_2$ reacted to form an Mg-Al-OH layered double hydroxide. These results demonstrate that encapsulation of Magnox sludge waste streams could be carried out in these alternative binders, but that the binders would

encapsulate rather than chemically incorporate the $Mg(OH)_2$ into the wasteform unless low SiO_2/Al_2O_3 ratios are used.

Keywords: Magnox sludge, cementation, brucite, zeolite

1. Introduction

During the past 60 years, the UK has relied on Magnox nuclear power plants for a significant portion of its electricity supply. These are CO_2 cooled, graphite moderated reactors using natural uranium fuel clad in a magnesium alloy (Magnox), of which 26 reactor units were constructed and operated in the UK. Cooling and reprocessing of spent fuel from these reactors has, over half a century, resulted in the accumulation of significant quantities of corrosion products and sludge due to degradation of the magnesium alloy fuel cladding during storage in cooling ponds and silos. This sludge consists primarily of $Mg(OH)_2$ with small quantities of hydrotalcite and artinite [1-2], along with an assortment of radioactive fission products and metallic residues. The radioactivity of this sludge is such that it is classified as Intermediate Level Waste (ILW), requiring conditioning by solidification in an appropriate matrix prior to disposal. Ongoing decommissioning of legacy facilities containing this type of sludge has reinforced the need for research into suitable encapsulation methods, to ensure that suitable potential immobilisation or encapsulation matrices are available for deployment in the safe and cost-effective disposal of these wastes.

Typically in the UK, ILW waste streams are conditioned within composite cements consisting of a blend of either blast furnace slag (BFS) or fly ash (FA), with Portland cement (PC) [3-4]. The chemistry of these blended cements is well understood, with decades of operational usage in waste cementation. These grouts have been assessed for immobilisation of Magnox sludges, and give solid monoliths with little reaction between the cementitious components and the sludge at early ages [5-6]. Within the principal strength-giving phase in Portland cements, a calcium silicate hydrate (C-S-H) type gel, there is little uptake of magnesium. Under specific conditions both C--S-H and magnesium silicate hydrate (M-S-H) type gels can form, though at the higher pH levels achieved within undamaged PC systems, magnesium is likely to remain as $Mg(OH)_2$ [7-8]. This is in line with the known limited solubility of $Mg(OH)_2$ in alkaline media, although the longer term reactivity of $Mg(OH)_2$ within these systems has not yet been quantified. Although such grouts can safely encapsulate the wastes, this method is not optimal in reducing the overall volume of waste packages, as only moderate quantities of the sludges can be encapsulated without hindering the hardening of the wasteform [6].

In an earlier study by the authors [9], cementitious binders within the $Mg(OH)_2$-$NaAlO_2$-SiO_2-H_2O system were studied up to 90 days of age, and the formation of a range of zeolites was identified, depending on the Si/Al ratio. Although the inclusion of $NaAlO_2$ significantly reduced the setting time of these binders, there was no evidence for M-S-H gel formation, with or without Al substitution. Instead, a layered double hydroxide with a hydrotalcite-like structure was observed in one of the formulations assessed, and it was noted that this may be potentially valuable in binding radionuclides, in particular I^- and TcO_4^- along with Cs^+ and Sr^{2+} [10-11], of which significant quantities exist within Magnox sludge [12].

The utilisation of $Mg(OH)_2$ as a raw material reacting to form a binding phase could potentially enable a reduction in wasteform volume compared to the current baseline grout formulations. Other alternative cements are able to perform in this way, however they also have certain disadvantages. Magnesium-oxysalt cements such as oxychloride or oxysulfate cements are deleteriously affected by water [13-14], severely reducing their scope for use as wasteforms. Magnesium phosphate cements (i.e. those based on struvite / struvite-K) typically require low-reactivity MgO as a raw material, suffering from flash setting when produced from $Mg(OH)_2$ [15]. Recently, magnesium silicate based cements have been produced by blending $Mg(OH)_2$ with reactive silica (in contrast to more common synthesis routes based on MgO); with extended curing at 40 °C, these blends form a M-S-H type gel as the sole binding phase, totally consuming the $Mg(OH)_2$, although with significantly slower setting times than are observed for Portland based grouts [16].

This study further evaluates phase evolution in $Mg(OH)_2$-SiO_2-$NaAlO_2$-H_2O samples cured for up to 2 years, to identify whether this combination of mix components may be tailored to achieve desirable long-term characteristics. Fresh pastes were assessed through isothermal calorimetry, while fresh (up to 120 h cured) and aged (up to 2 years cured) hardened specimens were characterised via X-ray diffraction, thermogravimetry coupled with mass spectrometry, and solid state ^{27}Al, ^{29}Si and ^{25}Mg magic angle spinning nuclear magnetic resonance (MAS NMR) spectroscopy.

2. Experimental methodology

2.1. Materials and sample preparation

As the principal raw materials, silica fume (Microsilica 940-U, Elkem, >90% SiO_2), sodium aluminate ($NaAlO_2$, technical grade, Fisher Scientific), $Mg(OH)_2$ (>95% purity, Alfa Aesar) and distilled water were used. Surface area and particle size distribution were determined by laser diffraction: $Mg(OH)_2$ surface area 3565 m^2/kg (D_{10} 0.7μm, D_{50} 4.2μm, D_{90} 29.0μm), silica fume 718 m^2/kg (D_{10} 4.4μm, D_{50} 20.0μm, D_{90} 118μm), indicating some degree of agglomeration between the particles.

Samples were formulated with a fixed quantity of $Mg(OH)_2$, but varying quantities of SiO_2 and $NaAlO_2$ to progressively increase the SiO_2/Al_2O_3 molar ratio. Samples are labelled by their SiO_2/Al_2O_3 molar ratios (R*x*, where *x* is between 1.3 and 3.3). The water / solids mass ratio (w/s) was kept constant at 0.6. The binder compositions are shown in Table 1.

Table 1. Formulations of samples studied within the $Mg(OH)_2$-$NaAlO_2$-SiO_2-H_2O system. Values are reported on a molar basis.

Sample ID	$Mg(OH)_2$	SiO_2	$NaAlO_2$	SiO_2/Al_2O_3 molar ratio
R1.3	3.0	1.0	1.5	1.3
R2.0	3.0	1.5	1.5	2.0
R3.0	3.0	1.5	1.0	3.0
R3.3	3.0	2.5	1.5	3.3

To produce each cement sample, dry powders were mixed together by hand to produce a homogeneous blend, to which the required quantity of distilled water was added to achieve w/s = 0.6, and further mixed for 5 minutes to produce a workable paste. Samples were cast into 15 mL centrifuge tubes and cured at 40 °C and 95% relative humidity in a Sanyo Atmos Chamber MTH-2400, until analysis.

2.2. Tests conducted

Isothermal calorimetry was undertaken for fresh pastes using a TAM Air calorimeter (TA Instruments) at 40 °C. Raw materials and water were preheated to 40 °C using an oven, then mixed externally and weighed into a polymeric (HDPE) ampoule. This was placed into the calorimeter, and the heat output measured for 30 days (720 hours), with heat flow normalized to the total sample mass (unless otherwise noted) in each sample.

Hardened paste samples were removed from the curing chamber at specified ages, and dried in a vacuum desiccator (13.3 kPa) over silica gel and solid NaOH for 6 hours to ensure the cessation of reaction and the removal of adsorbed water. Samples were then ground in an agate mortar and sieved to -63 μm for analysis.

X-ray diffraction analysis of young (24, 65 and 120 h cured) and aged (2 years cured) specimens was undertaken using a STOE STADI P diffractometer (Cu Kα radiation, 1.5418Å) with an image plate detector (IP-PSD), collecting data between 3.5-60° 2θ. Data were angle corrected using an external silicon standard (NIST 640d).

Thermogravimetric analysis (TGA) was carried out using a Perkin Elmer TGA 4000 coupled with a Hiden Analytical mass spectrometer. The mass spectrometer signals for H_2O and CO_2 were continuously recorded. The samples were assessed at a heating rate of 5ºC/min up to 900 ºC, using alumina crucibles and nitrogen as a purge gas (20 mL/min).

^{27}Al and ^{29}Si MAS NMR spectroscopy was performed on a Varian VNMRS 400 (9.4 T) spectrometer. ^{27}Al MAS NMR spectra were collected at 104.198 MHz, spinning at 14 kHz (12 kHz for 720 day samples) using a 4 mm o.d. zirconia rotor with a pulse duration of 1.0 μs, acquisition time of 10 ms and a recycle delay of 0.2 s, for a minimum of 1900 scans. Chemical shifts were referenced to 1.0 M aqueous $Al(NO_3)_3$. ^{29}Si MAS NMR spectra were collected at 79.435 MHz at a spinning speed of 6.8 kHz (6 kHz for 720 day samples) with a pulse duration of 6.2 μs (4.5 μs for 720 day samples), acquisition time of 20 ms (30 ms for 720 day samples) and a recycle delay of 60 s, for a minimum of 47 scans (912 for 720 day samples). Chemical shifts were externally referenced to tetramethylsilane (TMS) at 0 ppm. ^{25}Mg MAS NMR spectra were collected on a Bruker Avance III 850 (19.96 T) spectrometer using 4 mm o.d zirconia rotors, collected at 52.042 MHz at a spinning speed of 10.0 kHz, pulse duration of 5.0 μs and recycle delay of 2.0 s, for 5800 scans. Simulations were performed using Bruker Topspin 3.2 software. Chemical shifts were externally referenced to MgO.

3. Results and discussion

3.1 Early-age reaction processes

Calorimetric measurements were undertaken for samples R1.3, 2.0, 3.0 and 3.3 to determine the kinetics of reaction of binders within the $Mg(OH)_2$-$NaAlO_2$-SiO_2-H_2O system, and the processes which lead to solidification. All samples reacted in a strongly exothermic manner upon initial mixing, and formed viscous pastes. In the heat release curves (Figure 1) it is identified that each sample exhibits four distinct regions of interest, <1 h, 1-20 h, 20-70 h and 70-140 h. The region <1 h, corresponding to the induction period, shows the heat release associated with a combination of instrumentation effects due to emplacement of samples, and the initial dissolution of $NaAlO_2$ (followed by the heat of solution for NaOH formed [17-18]) which produced pastes that were notably hot to touch within minutes of mixing.

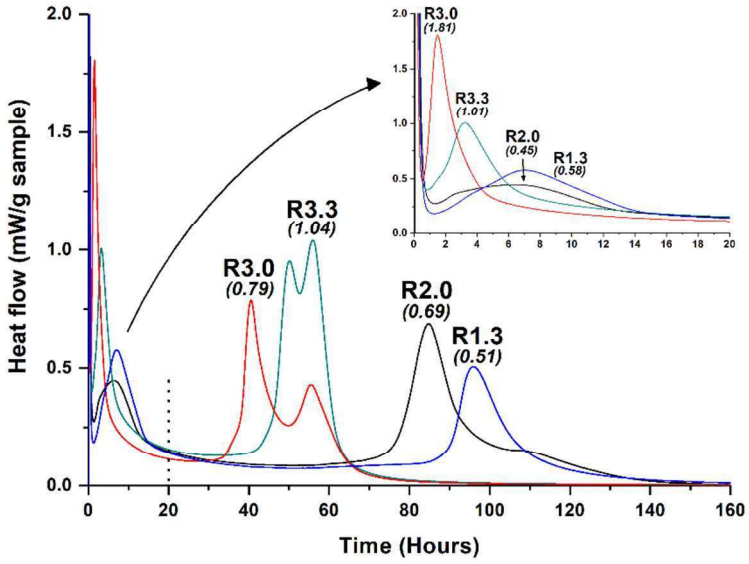

Figure 1. Normalised heat flow of fresh pastes within the systems $Mg(OH)_2$-$NaAlO_2$-SiO_2-H_2O (peak heat flow marked in parentheses)

Each of the samples exhibited an exothermic peak in the region 1-20 hours (with R3.0 and R3.3 exhibiting earlier, sharper heat output peaks than R2.0 and R1.3), which is assigned to dissolution of $NaAlO_2$, alkaline dissolution of SiO_2 and initial precipitation of $Al(OH)_3$, discussed in more detail below. This is followed by a dormant or induction period of low heat output, lasting 20-60 hours. After the dormant period, a high intensity peak corresponding to the acceleration-deceleration stage of the reaction was observed. During this stage a significant nucleation and growth of reaction products must be occurring in the samples assessed.

The time of onset of the acceleration period changes significantly upon lowering the SiO_2/Al_2O_3 ratio of these binders. The acceleration-deceleration period for samples with a higher silica content (R3.3 and R3.0) is observed between 30-60 hours. The formation of two overlapping but distinct heat release peaks indicates that different types of reaction products are precipitating at different times during the reaction process. Conversely, in samples containing less silica (R2.0 and R1.3), the second peak is less distinct, resulting in a single asymmetric peak observed after 75 to 150 hours of reaction, which appears latest in R1.3, the sample with the lowest silica content among the samples tested.

To identify the phases forming at the early stages of the reaction of these binders, X-ray diffraction (XRD) analysis was carried out on pastes cured under identical conditions to those used during the calorimetry test, at times where the higher rates of heat release were identified (24, 65 and 120 hours). After 24 h of reaction (Figure 2A), the only crystalline phases identified in these binders were unreacted brucite ($Mg(OH)_2$, powder diffraction file (PDF) # 01-074-2220) and traces of poorly crystalline bayerite (α-$Al(OH)_3$, PDF # 00-020-0011). No crystalline

$NaAlO_2$ is observed, indicating that this compound has fully dissolved, resulting in $Al(OH)_3$ precipitation, nor is any remnant SiO_2 observed (although as it is non-crystalline, identification of this phase amongst crystalline peaks is more challenging). This indicates that the first calorimetric peak at very early age is related, at least in part, to $NaAlO_2$ dissolution and the precipitation of this phase.

No differences in the diffraction patterns of R1.3 and R2.0 are identified (Figure 2B) after 65 hours compared to 24 hours, consistent with the identification of a dormant period in these pastes, spanning this period of time. Conversely, in samples R3.0 and R3.3 with higher silica content, the precipitation of zeolites of the structure type LTA (zeolite NaA: $Na_{12}Si_{12}Al_{12}O_{48}{\cdot}27H_2O$, PDF# 00-039-0219) is observed, which can explain the exothermic event identified via isothermal calorimetry. XRD analysis after 120 hours of reaction (Figure 2C) shows the formation of the LTA zeolite in all of the samples assessed. Regardless of chemical composition, after the initial reaction takes place in these binders, the main crystalline reaction products identified are $Al(OH)_3$ and LTA.

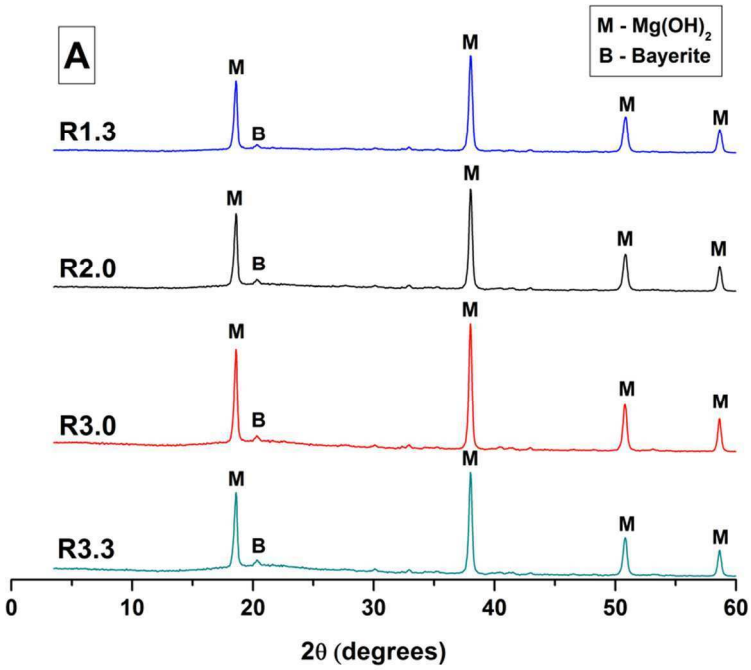
A
M - Mg(OH)2
B - Bayerite
R1.3
R2.0
R3.0
R3.3
M
B
0
10
20
30
40
50
60
2θ (degrees)

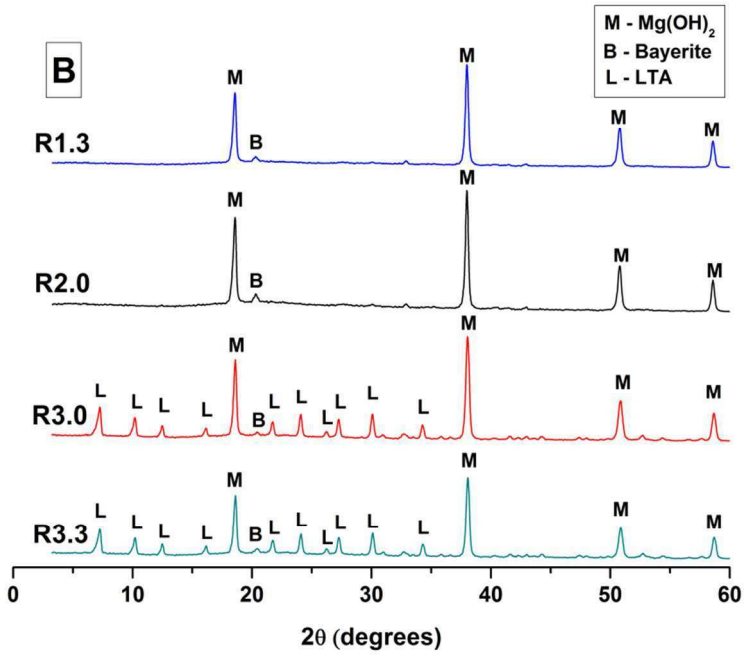
B
M - Mg(OH)2
B - Bayerite
L - LTA
R1.3
R2.0
R3.0
R3.3
M
B
L
0
10
20
30
40
50
60
2θ (degrees)

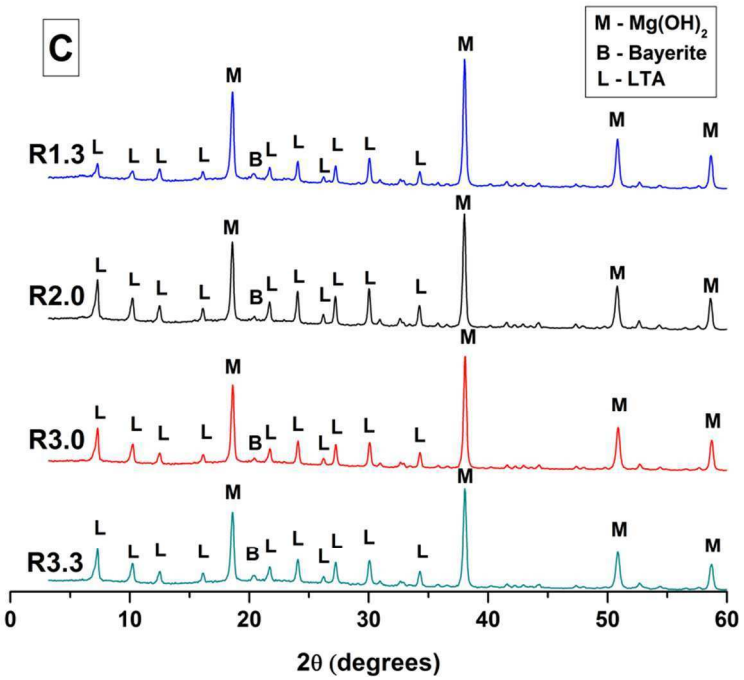

Figure 2. X-ray diffraction patterns of samples R1.3, 2.0, 3.0 and 3.3 after (A) 24, (B) 65 and (C) 120 hours of curing.

Cumulative heat release curves normalised to the total mass of paste (Figure 3) show that the heat released is dominated by the reaction between SiO_2 and $NaAlO_2$ to form LTA, with some contribution from excess $NaAlO_2$. Given the composition of LTA ($Na_{12}Si_{12}Al_{12}O_{48}{\cdot}27H_2O$), sample R2.0 results in the highest heat generation as this can produce the most LTA per gram: 15 mol SiO_2 + 15 mol $NaAlO_2$ yields 1.25 mol LTA. In both R1.3 and R3.0 less LTA is produced, as the reacting mix is off-stoichiometric (e.g. R1.3 has 10 mol SiO_2 to 15 mol $NaAlO_2$, yielding 0.83 mol LTA). The difference in heat output between R1.3 and R3.0 must be due to heat from processes involving excess reactants, suggesting that the dissolution and then reprecipitation (as $Al(OH)_3$) of excess $NaAlO_2$ produces additional heat. R3.3 can produce as much LTA as R2.0, but has an excess of SiO_2, reducing overall heat output per gram as this does not undergo a reaction process.

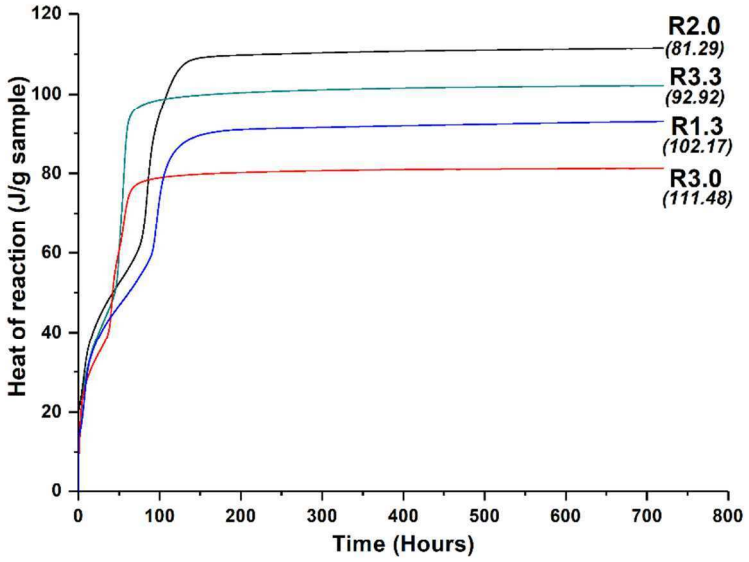

Figure 3. Cumulative heat of reaction of pastes within the system $Mg(OH)_2$-$NaAlO_2$-SiO_2-H_2O, normalized to the total mass of paste in each case. Total heat of reaction (J/g) in parentheses.

3.2 X-ray diffractometry of aged samples

The diffractograms of samples R1.3-R3.3 after 28, 360 and 720 days of curing are shown in Figure 4. Each of the samples displays an array of crystalline zeolites that varies depending on the formulation. After 28 days of curing, the higher SiO_2/Al_2O_3 samples R3.0 and R3.3 exhibit only LTA and $Mg(OH)_2$ as crystalline features, along with an amorphous component presenting a broad feature around 20° 2θ. The samples, R1.3 and R2.0 also contain additional Na-X (low silica faujasite: $Na_{86}Si_{106}Al_{86}O_{384}\cdot 175H_2O$, PDF# 00-012-0246, IZA zeolite framework type FAU). In sample R1.3, the LTA observed after 120 h (Figure 2C) was not longer observed at 28 days, with only Na-X, $Mg(OH)_2$ and traces of a sodalite-type structure. This corresponds to basic

hydrosodalite according to the nomenclature of Engelhardt et al.[19] ($Na_8Al_6Si_6O_{24}(OH)_2 \cdot 2H_2O$, PDF# 04-009-2429, IZA zeolite framework type SOD).

After longer curing times, the trends in the zeolite assemblages within these samples diverge. Samples R3.0 and R3.3 (Figure 4) do not show any changes in crystalline composition up to 720 days of curing, displaying considerable stability. However, samples R1.3 and R2.0, with lower SiO_2/Al_2O_3 ratios, do show significant changes. Sample R2.0 shows a change in zeolite mineralogy, with basic hydrosodalite and Na-P1 appearing after 360 days of curing, coinciding with a decrease in the intensity of LTA peaks. After 720 days no LTA remained, and the system is dominated by basic hydrosodalite along with some Na-P1 ($Na_6Al_6Si_{10}O_{32} \cdot 12H_2O$, PDF# 04-009-5257, IZA framework type GIS) and Na-X.

The transient nature of LTA in samples R1.3 and R2.0 can be explained by the fact that their lower SiO_2/Al_2O_3 ratios are achieved through a high $NaAlO_2$ content, which also results in more alkaline conditions within the pore fluid of these binders compared to the higher-silica R3.0 and R3.3. The LTA framework is also known to transform into sodalite type phases [20-22] and/or Na-P1 [23-25] in caustic media, although the process is slower in these cements, possibly due to the limited ionic mobility under the relatively low water/solids ratios used here compared to a regular hydrothermal synthesis process.

Sample R1.3, with the lowest SiO_2/Al_2O_3 ratio, undergoes a transformation whereby Na-X decreases in intensity, and basic hydrosodalite emerges as the dominant aluminosilicate phase. In addition to this, a hydrotalcite-like Mg-Al layered double hydroxide (LDH), potentially true

hydrotalcite ($Mg_6Al_2CO_3(OH)\cdot 4H_2O$, PDF# 00-054-1029) or a related structure differing in Mg/Al ratio or interlayer anions, forms by 360 days, increasing in intensity slightly at 720 days of curing. The identity of this phase will be further examined in Section 3.3, as hydrotalcite-group phases are challenging to distinguish from XRD data of moderate resolution as is the case here.

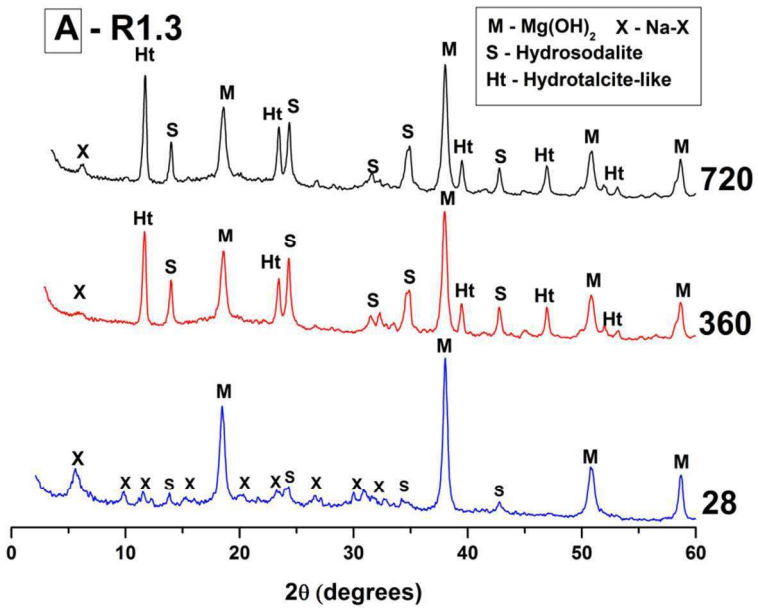

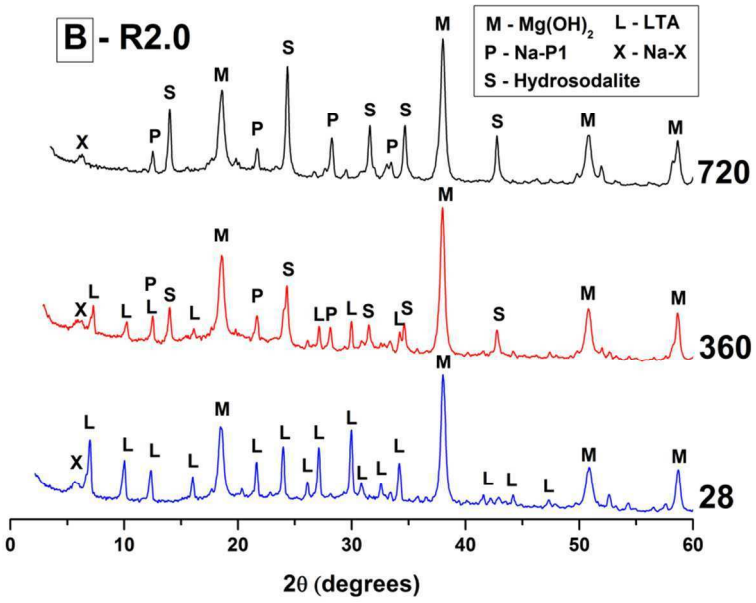
B - R2.0
M - Mg(OH)2 L - LTA
P - Na-P1 X - Na-X
S - Hydrosodalite
720
360
28
2θ (degrees)

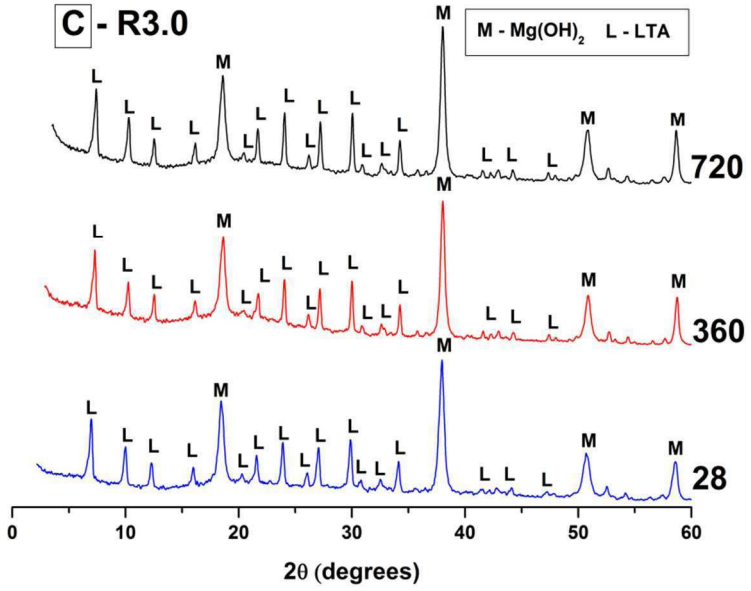
C - R3.0
M - Mg(OH)2 L - LTA
720
360
28
2θ (degrees)

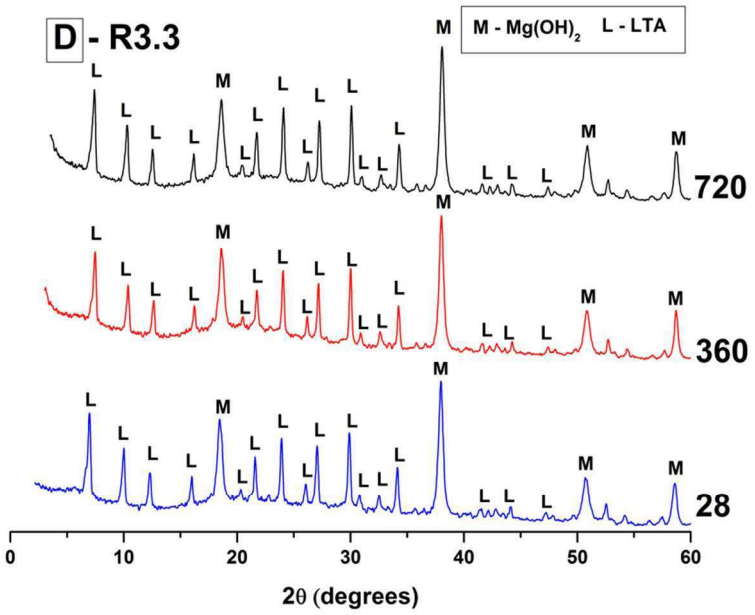

Figure 4. X-ray diffractograms of samples (A) R1.3, (B) R2.0, (C) R3.0 and (D) R3.3 as a function of the curing time in days (as marked). Some of the 28 day data are from [9].

Although sample R1.3 forms this additional magnesium-containing phase, all of the samples display strong reflections for $Mg(OH)_2$, suggesting that little reaction between the aluminosilicate components and $Mg(OH)_2$ has occurred up to 720 days of curing, except in R1.3. No evidence for the presence of an M-S-H phase can be detected (this would typically be identified from broad features at 20, 35 and 60° 2θ [7, 16]), even in the mixture R3.3 which was formulated to provide a large quantity of SiO_2 available for reaction.

3.3 Layered double hydroxide identification by thermal analysis

Although a layered double hydroxide (LDH) phase was identified during XRD analysis, the LDH family can encompass a wide range of compositions defined by the formula $[M^{2+}_{1-x}M^{3+}_{x}(OH)_2]^{x+}[A^{n-}_{x/n}]\cdot mH_2O$, in which M^{2+} and M^{3+} are di- and tri-valent metallic ions

respectively, and A^{n-} can be one of many anions (e.g. CO_3^{2-}, OH^-, Cl^-) [26]. For brevity this was labelled a 'hydrotalcite-like' phase in Figure 4, however as the samples were cured in a sealed container, this is likely to preclude much CO_2 ingress leading to formation of true (carbonate-containing) hydrotalcite. To determine the nature of this LDH, thermogravimetric analysis was undertaken with an attached mass spectrometer to distinguish between H_2O and CO_2 evolution, as shown in Figure 5.

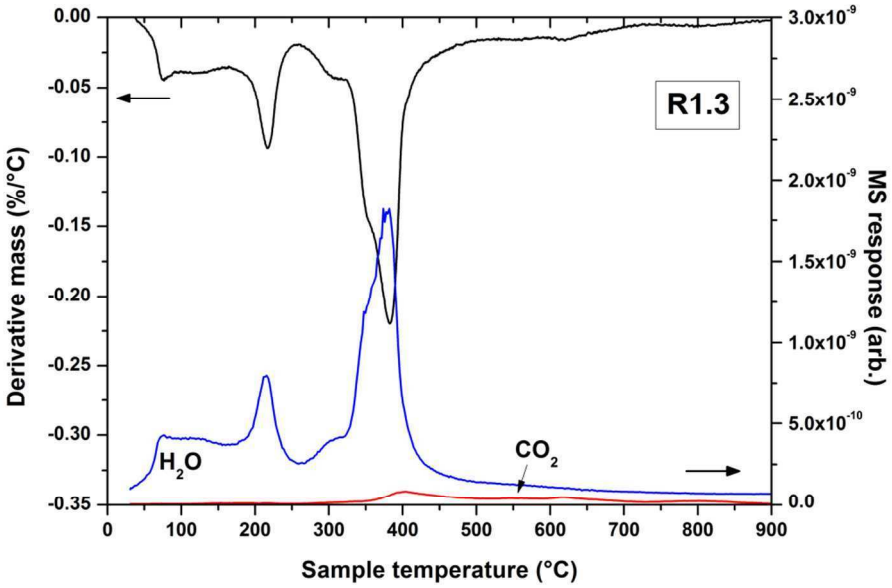

Figure 5. TG-MS data for sample R1.3 after 720 days curing, showing DTG (black), H_2O signal (blue) and CO_2 signal (red)

The multiple phases observed by XRD analysis (Figure 5) within sample R1.3 result in a complex TG-MS response in Figure 5. The mass loss is dominated by the decomposition of $Mg(OH)_2$ at 383°C [27], and by an Mg-Al layered double hydroxide containing hydroxyl species in the interlayer (denoted OH-LDH) which accounts for much of the remaining mass change, with characteristic decomposition peaks at ~90 °C, ~200 °C, and as shoulders on the $Mg(OH)_2$

decomposition peak at ~300°C and 350°C [28], suggesting that this phase may have a composition similar to $Mg_4Al_2(OH)_{18}{\cdot}mH_2O$, akin to a carbonate-free form of quintinite. It is likely that the Mg/Al ratio is at the lower end of the range associated with hydrotalcite-group phases (between 2 and 3) due to the limited reactivity of the $Mg(OH)_2$ and excess of $Al(OH)_3$ here. Some mass loss from bound water is also attributed to the release of zeolitic water from Na-X (~167°C) as well as dehydration of hydrosodalite, which decomposes slowly over a wide range, from ~80-750 °C [29-30]. A small signal for CO_2 is, however, observed at ~400°C, pointing to some formation of CO_2-containing LDH [31-32] as a minor constituent.

3.4 Solid-state NMR spectroscopy

Although various crystalline phases have formed within these cements, the presence of diffuse scattering in many of the XRD patterns (e.g. at ~20° 2θ in Figure 4C and D) suggests either that unreacted silica fume remains, or that non-crystalline reaction products are forming. To further elucidate this, ^{27}Al and ^{29}Si MAS NMR spectra were measured for all of the samples after 360 and 720 days of curing. The 360-day data are shown in Figure 6.

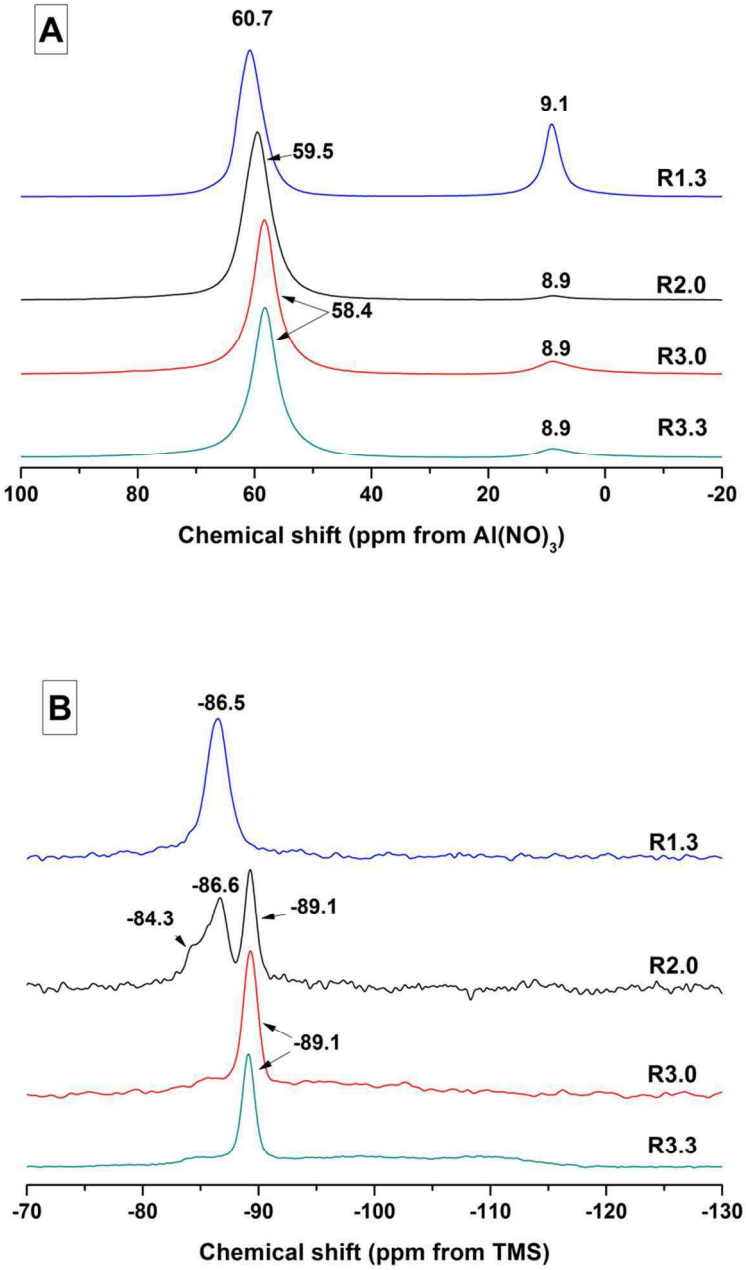

Figure 6. (A) ^{27}Al and (B) ^{29}Si MAS NMR spectra of pastes within the system $Mg(OH)_2$-$NaAlO_2$-SiO_2-H_2O, after 360 days of curing

The ^{27}Al MAS NMR spectra of the samples, Figure 6A, reveal the presence of two Al environments, identified as Al(IV) and Al(VI), at 58-61 and ~9 ppm respectively. The peaks close to 60 ppm are characteristic of tetrahedrally coordinated Al in zeolites, consistent with the

formation of aluminosilicate zeolites in these samples [33]. The peaks at ~9 ppm correspond to octahedrally coordinated Al, typical of non-framework Al species. Sample R1.3 exhibits a stronger signal here, consistent with the identification of a hydrotalcite-like LDH as discussed above [34]. In the remaining samples, although LDH phases have not been observed through XRD analysis, the presence of this octahedral Al might be evidence of some small, poorly crystalline LDH phase, or perhaps the presence of Al(VI) might be evidence of residual α-$Al(OH)_3$ as postulated through XRD analysis earlier.

The ^{29}Si MAS NMR data in Figure 6B further support the identification of zeolites. The single peak at -89.1 ppm in samples R2.0-R3.3 is assigned to Q^4(4Al) units in the LTA framework [33, 35-36]. Sample R2.0 exhibits a more complicated spectrum, with an additional signal at -86.6 ppm from Q^4(4Al) units in the sodalite framework structure [19, 36], and a small signal at -84.3 ppm associated with Q^4(4Al) units in low silica Na-X [35]. R1.3 exhibits a single peak at -86.5 ppm, consistent with the identification of the sodalite framework type as the primary zeolite at this age by XRD, Figure 4.

High field ^{25}Mg MAS NMR spectra were also collected to clarify the role of Mg within this binding system. These data are shown in Figure 7 for sample R3.3 at 360 days of curing. The experimental data were fitted with simulations based on established literature values for magnesium minerals [16, 37] (Table 2), and found to represent predominantly $Mg(OH)_2$, with some MgO present as an impurity. M-S-H would present a diffuse resonance centred at ~0 ppm at this field strength [16]. As the experimental data can be fitted well using a simulation describing $Mg(OH)_2$ and MgO alone, no M-S-H can be said to exist within this sample. Equally, as no other

Mg sites are observable, the formation of an Al-bearing M-A-S-H phase can also be excluded. Unfortunately, restricted access to in-demand equipment precluded the collection of data for sample R1.3 which contains hydrotalcite-group phases

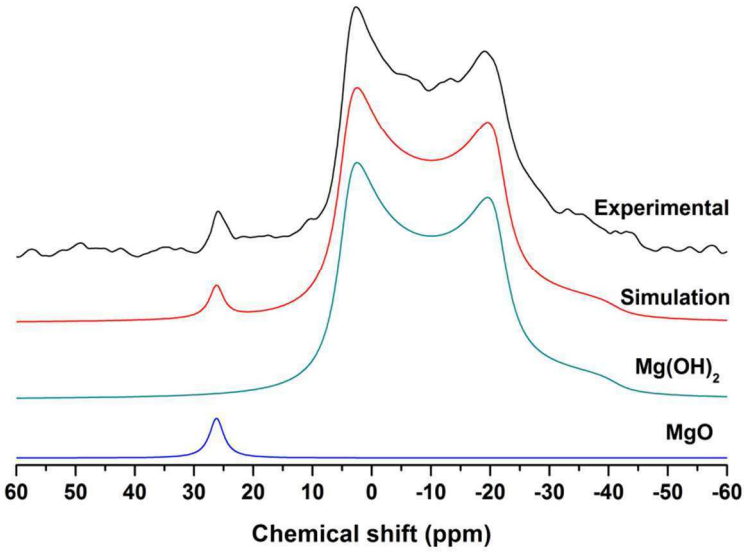

Figure 7. ^{25}Mg MAS NMR spectra of sample R3.3 at 360 days of curing, with experimental data, simulation, and component peaks

Table 2. ^{25}Mg MAS NMR simulation parameters for R3.3 at 360 days of curing

	δ_{iso} (ppm)	C_Q (MHz)	η_Q
MgO	26.2	0	0
$Mg(OH)_2$	11.7	3.1	0

All of the samples were analysed again after curing for 720 days, to determine whether there were any further changes over time. The NMR spectra remained similar for samples R3.0 and

R3.3, with only minor shifts in peak positions in both ^{27}Al and ^{29}Si MAS NMR (Figure 8). These samples all exhibit broad signals in their ^{29}Si spectra, and are deconvoluted in Figure 9. Samples R1.3 and R2.0, however, do show changes from 360 to 720 days, consistent with their changing zeolite assemblages identified by XRD (Figure 5). In sample R1.3, a second peak appeared at -84 ppm, consistent with an increase in the observed Na-X content, while in sample R2.0 the peak at -86.5 ppm (identified as sodalite) increased in intensity, while that assigned to LTA (-89.1 ppm) disappeared entirely; both of these trends are in full agreement with the XRD assignments.

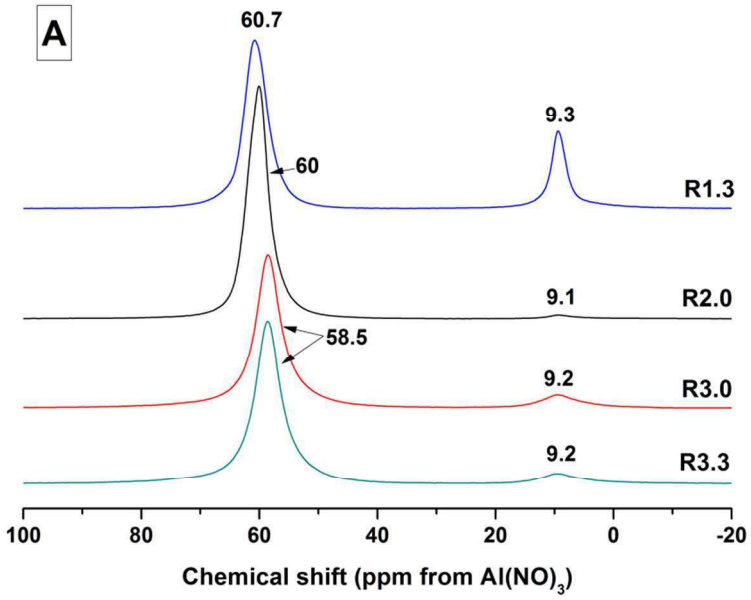

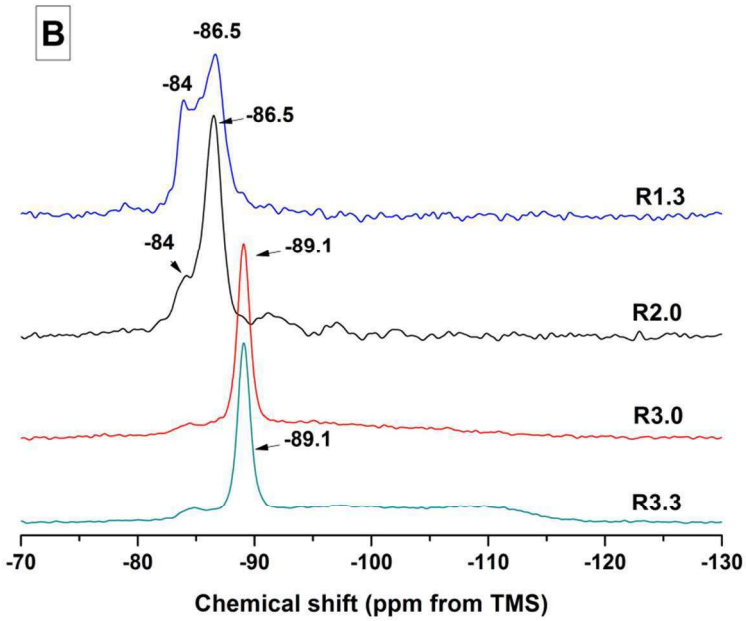

Figure 8. (A) ^{27}Al and (B) ^{29}Si MAS NMR spectra of pastes within the system $Mg(OH)_2$-$NaAlO_2$-SiO_2-H_2O, after 720 days of curing

Deconvolution was undertaken on the ^{29}Si MAS NMR spectra for samples R3.0 and R3.3, which both display broad features. Alongside the prominent peak at -89.1 ppm, assigned to LTA (Q^4(4Al)), are four additional broad peaks centred -85.8, -92.7, -99.6 and -109.3 pm. The peak at -109.3 ppm can be assigned to fully polymerised Q^4 species in unreacted silica fume. The next peak downfield, at -99.6 ppm, is assigned to Q^3 species formed through surface hydroxylation of the silica fume due to partial dissolution, forming Q^3 (>Si-OH single silanol) sites surrounding an unreacted Q^4 silica fume core [38]. The two remaining peaks at -92.7 and -85.8 ppm are assigned to Q^3(1Al) and Q^2(1Al) sites respectively. Both of these sites occur as the $Al(OH)_4^-$ released by sodium aluminate dissociation form either surface Q^3(1Al), or further depolymerised Q^2(1Al) units.

In general, there appears to be a larger contribution from the disordered phases within R3.3 than R3.0 (assuming no substantive change in the ^{29}Si T_1 relaxation time between samples), suggesting that a higher SiO_2/Al_2O_3 ratio in the formulation favours an increased fraction of the Q^4, Q^3 and Q^3(1Al) sites, while a lower SiO_2/Al_2O_3 content results in a larger contribution from the Q^4(4Al) site of LTA. With a higher silica content, more unreacted silica is contributing to the spectrum, along with hydroxylated and aluminated silica surface sites. Overall there is no evidence of a M-S-H or M-A-S-H type phase forming, despite the presence of unreacted and partially aluminated silica. As this has not occurred within 2 years of curing, it is concluded that Mg incorporation into silicate phases is unlikely to occur in these samples within a meaningful engineering timeframe, and if this does eventually happen, the kinetics of the process are very slow compared to the zeolite formation.

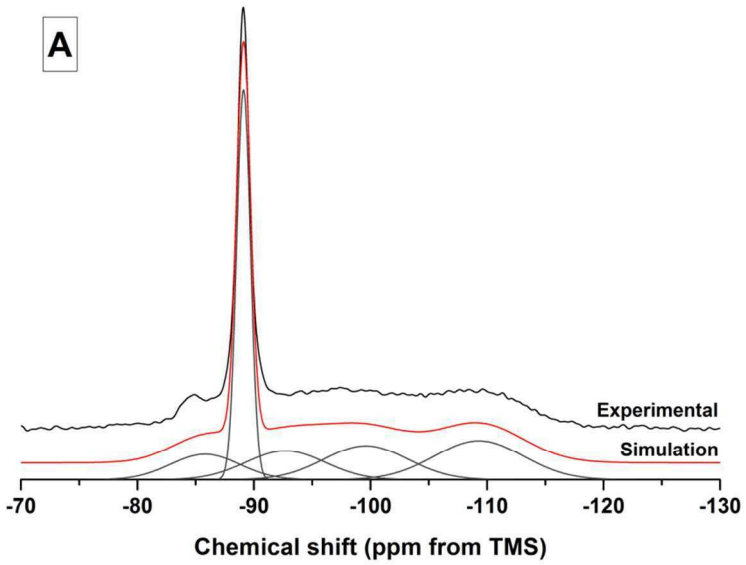

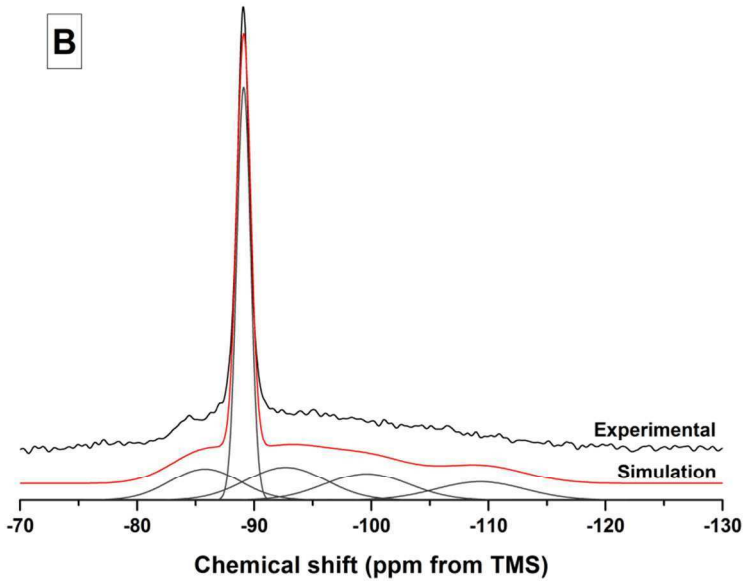

Figure 9. ^{29}Si MAS NMR spectra of samples (A) R3.3 and (B) R3.0 at 720 days of curing, featuring both experimental and simulated spectra, and decomposition into component peaks

4. Conclusions

The results of this study demonstrate the feasibility of producing an alternative cementitious system which can encapsulate and utilise very high mass fractions of $Mg(OH)_2$ as a constituent material. The addition of reactive $NaAlO_2$ into the $Mg(OH)_2$-SiO_2-H_2O system promotes the formation of mixed zeolites, the composition of which varies depending on the SiO_2/Al_2O_3 content of the samples.

Initially all samples precipitated $Al(OH)_3$, followed by zeolites after 20-60 hours. Higher SiO_2/Al_2O_3 ratios resulted in faster zeolite formation, although all samples initially exhibited strong heat output during mixing. All samples first formed LTA zeolite, before slowly showing

alterations in the zeolite assemblage over time. High SiO_2/Al_2O_3 ratios stabilized LTA, while lower ratios resulted in formation of a low silica faujasite (Na-X) zeolite, Na-P1, hydroxysodalite, and a hydrotalcite-type phase in the lowest SiO_2/Al_2O_3 ratio sample. This was determined through TG-MS analysis to be a hydroxide-containing layered double hydroxide with very limited carbonate incorporation, formed from some reaction of $Mg(OH)_2$ with the added $NaAlO_2$.

^{27}Al and ^{29}Si solid state MAS NMR spectroscopy confirmed the zeolite assignments from the XRD analysis, and also revealed unreacted silica fume, a hydroxylated Q^3 site and aluminated $Q^2(1Al)$ and $Q^3(1Al)$ sites, which were not detectable by XRD due to lack of long-range ordering. Further analysis using ^{25}Mg NMR was not able to detect any M-S-H or M-A-S-H formation, despite the presence of large quantities of both $Mg(OH)_2$ and SiO_2.

Although no M-S-H or M-A-S-H phases have been identified here, the addition of high quantities of $NaAlO_2$ promoted the formation of a magnesium-aluminium layered double hydroxide. Aside from this sample, none of the other formulations resulted in reacted $Mg(OH)_2$, which was encapsulated within the matrix rather than chemically bound. The potential for ion-exchange between the zeolites, the LDH and any radionuclides may be of benefit for the immobilisation of radionuclide bearing wastes, specifically Magnox sludges. U and Pu typically have very low solubility in high pH environment, often forming hydroxides [39]. Trivalent actinides (such as Am), though also exhibiting low solubility at high pH could incorporate into hydrotalcite minerals [39]. More problematic species such as Cs can be irreversible incorporated into sodalite and Na-P1 structures [40-41], while anions such as Cl^- and TcO_4^- could potentially

exchange with anionic species in hydrotalcite [42-44]. This would point towards the lowest SiO_2/Al_2O_3 ratio formulation, R1.3, potentially being preferable due to formation of a hydrotalcite-type mineral. However, ionic binding in hydrotalcites is often reversible, and dependent on existing anions [43, 45], and therefore deserves further study.

Acknowledgements

This study was sponsored by the Engineering and Physical Sciences Research Council (EPSRC) through the University of Sheffield/ University of Manchester Doctoral Training Centre 'Nuclear FiRST' (EP/G037140/1) and through a Nuclear Decommissioning Authority CASE award, under supervision by the National Nuclear Laboratory. The donation of microsilica by Elkem Silicon Materials is greatly appreciated. Solid-state NMR spectra for ^{27}Al and ^{29}Si were obtained at the EPSRC UK National Solid-state NMR Service at Durham. The UK 850 MHz solid-state NMR Facility used in this research to collect ^{25}Mg spectra was funded by EPSRC and BBSRC, as well as the University of Warwick including via part funding through Birmingham Science City Advanced Materials Projects 1 and 2 supported by Advantage West Midlands (AWM) and the European Regional Development Fund (ERDF). The assistance of Dr. David Apperley and Dr Dinu Iuga in NMR data collection is greatly appreciated. This research was performed in part at the MIDAS Facility, at the University of Sheffield, which was established with support from the Department of Energy and Climate Change.

References

1. Gregson, C. R.; Goddard, D. T.; Sarsfield, M. J.; Taylor, R. J., Combined electron microscopy and vibrational spectroscopy study of corroded Magnox sludge from a legacy spent nuclear fuel storage pond. *J. Nucl. Mater.* **2011,** *412* (1), 145-156.

2. Parry, S.; Livens, F.; O'Brien, L., Corroded Magnox sludge and plutonium waste cementation. *Geochim. Cosmochim. Acta* **2007,** *71* (15, Supplement), A747-A815.

3. Atkins, M.; Glasser, F. P., Application of portland cement-based materials to radioactive waste immobilization. *Waste Manag.* **1992,** *12* (2-3), 105-131.

4. Ojovan, M. I.; Lee, W. E., *An Introduction to Nuclear Waste Immobilisation*. Elsevier: Oxford, 2005.

5. Collier, N. C.; Milestone, N. B., The encapsulation of $Mg(OH)_2$ sludge in composite cement. *Cem. Concr. Res.* **2010,** *40* (3), 452-459.

6. Hough, T.; Palethorpe, S., Development of a direct encapsulation technique for the treatment of a mixed sludge / solid waste. In *WM'07 Conference*, Tucson, AZ, 2007.

7. Lothenbach, B.; Nied, D.; L'Hôpital, E.; Achiedo, G.; Dauzères, A., Magnesium and calcium silicate hydrates. *Cem. Concr. Res.* **2015,** *77*, 60-68.

8. Dauzeres, A.; Achiedo, G.; Nied, D.; Bernard, E.; Alahrache, S.; Lothenbach, B., Magnesium perturbation in low-pH concretes placed in clayey environment—solid characterizations and modeling. *Cem. Concr. Res.* **2016,** *79*, 137-150.

9. Walling, S. A.; Bernal, S. A.; Kinoshita, H.; Collier, N. C.; Provis, J. L., Cementitious binders in the system $Mg(OH)_2$–$NaAlO_2$–SiO_2–H_2O. *Adv. Appl. Ceram.* **2014,** *113* (8), 496-501.

10. Kulyukhin, S. A.; Krasavina, E. P.; Gredina, I. V.; Rumer, I. A.; Mizina, L. V., Sorption of cesium, strontium, and yttrium radionuclides from the aqueous phase on layered double hydroxides. *Radiochem. (Moscow)* **2008,** *50* (5), 493-501.

11. Kang, M. J.; Chun, K. S.; Rhee, S. W.; Do, Y., Comparison of sorption behavior of I^- and TcO_4^- on Mg/Al layered double hydroxide. *Radiochim. Acta* **1999**, *85*(1-2), 57-63.

12. Nuclear Decomissioning Authority (NDA) *Waste stream 2D95.1: Magnox fuel storage pond sludge*; NDA: 2016.

13. Urwongse, L.; Sorrell, C. A., Phase relations in magnesium oxysulfate cements. *J. Am. Ceram. Soc.* **1980,** *63* (9-10), 523-526.

14. Walling, S.; Provis, J., Magnesia based cements - a journey of 150 years, and cements for the future? *Chem. Rev.* **2016,** *116*, 4170-4204.

15. Kingery, W. D., Fundamental study of phosphate bonding in refractories: II, Cold-setting properties. *J. Am. Ceram. Soc.* **1950,** *33* (8), 242-246.

16. Walling, S. A.; Kinoshita, H.; Bernal, S. A.; Collier, N. C.; Provis, J. L., Structure and properties of binder gels formed in the system $Mg(OH)_2$-SiO_2-H_2O for immobilisation of Magnox sludge. *Dalton Trans.* **2015,** *44*, 8126-8137.

17. Bertetti, J. W.; McCabe, W. L., Sodium hydroxide solutions. *Ind. Eng. Chem.* **1936,** *28* (2), 247-248.

18. Lide, D. R., *CRC Handbook of Chemistry and Physics, 88th Edition*. CRC Press: Boca Raton, FL, 2007.

19. Engelhardt, G.; Felsche, J.; Sieger, P., The hydrosodalite system $Na_{6+x}[SiAlO_4]_6(OH)_x \cdot nH_2O$: Formation, phase composition, and de- and rehydration studied by ^{1}H, ^{23}Na, and ^{29}Si MAS-NMR spectroscopy in tandem with thermal analysis, X-ray diffraction, and IR spectroscopy. *J. Am. Chem. Soc.* **1992,** *114* (4), 1173-1182.

20. Subotić, B.; Škrtić, D.; Šmit, I.; Sekovanić, L., Transformation of zeolite A into hydroxysodalite: I. An approach to the mechanism of transformation and its experimental evaluation. *J. Cryst. Growth* **1980,** *50* (2), 498-508.

21. Walton, R. I.; Millange, F.; O'Hare, D.; Davies, A. T.; Sankar, G.; Catlow, C. R. A., An in situ energy-dispersive x-ray diffraction study of the hydrothermal crystallization of zeolite A. 1. Influence of reaction conditions and transformation into sodalite. *J. Phys. Chem. B* **2001,** *105* (1), 83-90.

22. Greer, H.; Wheatley, P. S.; Ashbrook, S. E.; Morris, R. E.; Zhou, W., Early stage reversed crystal growth of zeolite A and its phase transformation to sodalite. *J. Am. Chem. Soc.* **2009,** *131* (49), 17986-17992.

23. Subotić, B.; Šmit, I.; Madžija, O.; Sekovanić, L., Kinetic study of the transformation of zeolite A into zeolite P. *Zeolites* **1982,** *2* (2), 135-142.

24. International Zeolite Association Structure Commission (IZA-SC), *Collection of simulated XRD powder patterns for zeolites*. 4th ed.; Amsterdam, Netherlands, 2001.

25. Hansen, S.; Håkansson, U.; Landa-Canovas, A. R.; Falth, L., On the crystal chemistry of NaP zeolites. *Zeolites* **1993,** *13* (4), 276-280.

26. Mills, S. J.; Christy, A. G.; Génin, J.-M. R.; Kameda, T.; Colombo, F., Nomenclature of the hydrotalcite supergroup: natural layered double hydroxides. *Mineral. Mag.* **2012,** *76* (5), 1289-1336.

27. MacKenzie, K. J. D.; Meinhold, R. H., Thermal decomposition of brucite, $Mg(OH)_2$: a ^{25}Mg MAS NMR study. *Thermochim. Acta* **1993,** *230*, 339-343.

28. Valente, J. S.; Pfeiffer, H.; Lima, E.; Prince, J.; Flores, J., Cyanoethylation of alcohols by activated Mg–Al layered double hydroxides: Influence of rehydration conditions and Mg/Al molar ratio on Brönsted basicity. *Journal of Catalysis* **2011,** *279* (1), 196-204.

29. Felsche, J.; Luger, S., Phases and thermal decomposition characteristics of hydro-sodalites $Na_{6+x},[AlSiO_4]_6,(OH)_x \cdot nH_2O$. *Thermochim. Acta* **1987,** *118* (0), 35-55.

30. Joshi, U. D.; Joshi, P. N.; Tamhankar, S. S.; Joshi, V. P.; Idage, B. B.; Joshi, V. V.; Shiralkar, V. P., Influence of the size of extraframework monovalent cations in X-type zeolite on their thermal behavior. *Thermochim. Acta* **2002,** *387* (2), 121-130.

31. Constantino, V. R. L.; Pinnavaia, T. J., Basic properties of $Mg^{2+1-x}Al^{3+x}$ layered double hydroxides intercalated by carbonate, hydroxide, chloride, and sulfate anions. *Inorg. Chem.* **1995,** *34* (4), 883-892.

32. Kloprogge, J. T.; Kristóf, J.; Frost, R. L., Thermogravimetric analysis-mass spectrometry (TGA-MS) of hydrotalcites containing CO_3^{2-}, NO_3^-, Cl^-, SO_4^{2-} or ClO_4^-. In *2001. A clay odyssey. Proceedings of the 12th international clay conference*, Bahía Blanca, Argentina, 2001.

33. Engelhardt, G., Solid state NMR spectroscopy applied to zeolites. In *Studies in Surface Science and Catalysis*, van Bekkum, H.; Flanigen, E. M.; Jacobs, P. A.; Jansen, J. C., Eds. Elsevier: 2001; Vol. Volume 137, pp 387-418.

34. MacKenzie, K. J. D.; Meinhold, R. H.; Sherriff, B. L.; Xu, Z., ^{27}Al and ^{25}Mg solid-state magic-angle spinning nuclear magnetic resonance study of hydrotalcite and its thermal decomposition sequence. *J. Mater. Chem.* **1993,** *3* (12), 1263-1269.

35. Lippmaa, E.; Maegi, M.; Samoson, A.; Tarmak, M.; Engelhardt, G., Investigation of the structure of zeolites by solid-state high-resolution silicon-29 NMR spectroscopy. *J. Am. Chem. Soc.* **1981,** *103* (17), 4992-4996.

36. Newsam, J. M., Silicon-29 chemical shifts in sodalite materials. *J. Phys. Chem.* **1987,** *91* (5), 1259-1262.

37. Pallister, P. J.; Moudrakovski, I. L.; Ripmeester, J. A., Mg-25 ultra-high field solid state NMR spectroscopy and first principles calculations of magnesium compounds. *Phys. Chem. Chem. Phys.* **2009,** *11* (48), 11487-11500.

38. Zhuravlev, L. T., The surface chemistry of amorphous silica. Zhuravlev model. *Colloids Surf., A* **2000,** *173* (1–3), 1-38.

39. Nuclear Decomissioning Authority (NDA) *Geological Disposal: Radionuclide behaviour status report*; NDA 2010.

40. Mon, J.; Deng, Y.; Flury, M.; Harsh, J., Cesium incorporation and diffusion in cancrinite, sodalite, zeolite and allophane. *Microporous Mesoporous Mater.* **2005,** *86*, 277-286.

41. Penilla, R. P.; Guerrero Bustos, A.; Goñi Elizalde, S., Immobilization of Cs, Cd, Pb and Cr by synthetic zeolites from Spanish low-calcium coal fly ash. *Fuel* **2006,** *85* (5–6), 823-832.

42. Aggarwal, S.; Angus, M. J.; Ketchen, J. *Sorption of radionuclides onto specific mineral phases present in repository cements*; AEA Technology: Windscale 2000.

43. Bontchev, R. P.; Liu, S.; Krumhansl, J. L.; Voigt, J.; Nenoff, T. M., Synthesis, characterization, and ion exchange properties of hydrotalcite $Mg_6Al_2(OH)_{16}(A)_x(A')_{2-x}\cdot 4H_2O$ (A, A' = Cl^-, Br^-, I^-, and NO_3^-, $2 \geq x \geq 0$) derivatives. *Chem. Mater.* **2003,** *15* (19), 3669-3675.

44. Wall, N. A.; Minai, Y., Adsorption of $^{99}TcO_4^-$ onto hydrotalcite and calcined hydrotalcite under basic conditions: influence of humic acids and anions. *J. Radioanal. Nucl. Chem.* **2014,** *301* (1), 221-225.

45. Miyata, S., The syntheses of hydrotalcite-like compounds and their structures and physico-chemical properties - I: The systems Mg^{2+}-Al^{3+}-NO_3^-, Mg^{2+}-Al^{3+}-Cl^-, Mg^{2+}-Al^{3+}-ClO_4^-, Ni^{2+}-Al^{3+}-Cl^- and Zn^{2+}-Al^{3+}-Cl^-. *Clays Clay Miner.* **1975,** *23* (5), 369-375.

For Table of Contents Only